Monthly Notices of the ROYAL ASTRONOMICAL SOCIETY

MNRAS **547,** 1–17 (2026) https://doi.org/10.1093/mnras/stag267
Advance Access publication 2026 February 11

Multiwavelength morphology and dust emission in low-redshift dwarf galaxies in COSMOS-Web with *HST* and *JWST*

D. Kakkad [1★] I. Lazar [1] S. Harish,[2] B. Bichang'a [1] R. K. Cochrane [3] S. Kaviraj [1] A. E. Watkins,[1] G. Martin [4] S. Koudmani [1,5] Andrew J. Battisti,[6,7,8] Caitlin Casey,[9,10,11] Maximilien Franco,[12] G. Gozaliasl,[13,14] M. Hirschmann [15] Jeyhan Kartaltepe,[2] A. A. Khostovan [2,16] Anton Koekemoer [17] Daizhong Liu,[18] Henry Joy McCracken,[19] Jason Rhodes[20] and Brant Robertson[21]

Affiliations are listed at the end of the paper

Accepted 2026 February 6. Received 2026 January 21; in original form 2025 July 17

ABSTRACT

Low-mass or dwarf galaxies ($M_* < 10^9$ M$\odot$) are abundant in the Universe, yet their formation and evolution remain poorly understood. Their enhanced sensitivity to feedback from star formation and active galactic nuclei (AGNs) make them excellent laboratories to test whether feedback prescriptions in cosmological simulations accurately reproduce their interstellar medium (ISM) properties. We present *James Webb Space Telescope*/near-infrared camera (*JWST*/NIRCam) and mid-infrared instrument (MIRI) imaging of nine dwarf galaxies from COSMOS-Web survey at redshift $z < 0.08$, with star formation rates ranging from 0.003 to 0.3 M$\odot$ yr^{-1} and stellar masses of log $M_* \sim 8$–9 M$_\odot$. The detection rate with both NIRCam and MIRI is 100 per cent, indicating that these dwarfs possess substantial ISM content. The detected sample includes a roughly equal mix of early-type and late-type dwarfs, suggesting that it is representative of the broader dwarf galaxy population in low-density environments. We find that the observed MIRI flux distributions are comparable to forward-modelled flux distributions of mass-matched simulated galaxies in TNG50. We further conduct a multiwavelength morphological analysis complementing the *JWST* NIRCam and MIRI imaging with archival *Hubble Space Telescope*/Advanced Camera for Surveys (*HST*/ACS) data, employing the CAS (concentration, asymmetry, smoothness) framework. Among the multiwavelength images, MIRI exhibits the largest variation in CAS parameters, likely due to dust lanes and clumps in several galaxies, also suggested by spectral energy distribution (SED) fitting. This suggests that the dust content in these systems may be higher than those implied by rest-frame optical or near-infrared observations alone. Upcoming ultraviolet/optical and mid-infrared spectroscopic follow-up will be critical for constraining the gas kinematics and dust grain properties of dwarf galaxies in low-density environments such as COSMOS.

Key words: methods: observational – techniques: image processing – galaxies: dwarf – galaxies: evolution – galaxies: ISM – galaxies: structure.

1 INTRODUCTION

Luminosity or mass functions of galaxies suggest that low-mass or dwarf galaxies are the most abundant class of galaxies in the Universe (e.g. A. H. Wright et al. 2017). In a hierarchical universe, these low-mass galaxies merge and form more massive galaxies over cosmic time and therefore, studies focusing on the formation and evolution of dwarf galaxies offer valuable insights into the broader galaxy evolution process. The importance of dwarf galaxies in the Universe is further highlighted by recent works that suggest that dwarf galaxies may have contributed significantly in reionizing the Universe at high-redshifts (e.g. H. Atek et al. 2024). Due to their low mass, they have shallow potential wells and are therefore, more vulnerable to the effects of feedback from star formation and/or active galactic nuclei (AGNs), compared to massive galaxies (e.g. R. A. Jackson et al. 2021). This makes them ideal to test implementations of current feedback prescriptions in cosmological simulations (see M. Vogelsberger et al. 2020, for a review) by comparing the observed interstellar medium (ISM) content with predictions of low-mass galaxies in these simulations (e.g. G. Martin et al. 2025; A. E. Watkins et al. 2025). In fact, recent studies have indeed suggested that AGN may be more common in dwarf galaxies than previously thought (e.g. S. Kaviraj, G. Martin & J. Silk 2019; M. Mezcua et al. 2024) and therefore, a combination of feedback from star formation and AGN might add more energetic feedback into the ISM of dwarf galaxies (e.g. G. Dashyan et al. 2018; F. Davis et al. 2022; S. Koudmani, D. Sijacki &

★ E-mail: darshankakkad@gmail.com

M. C. Smith 2022; C. Partmann et al. 2024; J. Petersson et al. 2025). As a result, different feedback prescriptions (the relative strength of AGN versus star formation feedback, coupling efficiencies) may produce a different ISM composition, which can be directly tested with imaging and spectroscopic observations.

Despite being abundant, dwarf galaxies are not targeted for high-resolution imaging or spectroscopy in as much detail as their massive counterparts, partially because of their low surface brightness. For massive galaxies, follow-up observations with even 2m-class telescopes can readily target large statistical samples. However, the low surface brightness of most dwarf galaxies poses challenges for high-resolution imaging and spectroscopic follow-up of similarly large samples. As a result, key questions surrounding the formation and evolution of these dwarfs, such as their star formation history, ISM content (metallicity, multiphase gas mass), presence of outflows, morphological mix, are being actively studied. In particular, it is still unclear how the interplay between the star formation and AGN feedback shape the ISM of dwarf galaxies and to what extent does AGN affect star formation in dwarf galaxies? In other words, is the current implementation of feedback in simulations sufficient to reproduce the ISM of low-mass or dwarf galaxies?

Most studies in the literature targeting dwarf galaxies have been biased towards nearby systems or special classes of dwarf galaxies that inherently bias samples towards higher star formation rates (SFRs). Examples of such studies include targets in high-density environments, such as galaxy clusters (e.g. R. Sánchez-Janssen, J. A. L. Aguerri & C. Muñoz-TuñR. ón 2008; L. Ferrarese et al. 2012; P. Eigenthaler et al. 2018; A. Venhola et al. 2019), nearby dwarf galaxies (e.g. D. A. Dale et al. 2006) or dwarfs within the Local Group (e.g. E. Tolstoy, V. Hill & M. Tosi 2009; A. W. McConnachie 2012; D. R. Weisz et al. 2014), dwarf satellites surrounding massive galaxies (e.g. I. Trujillo et al. 2021) or specific classes such as blue compact dwarfs (BCDs; e.g. P. Papaderos et al. 1996; Y. Wu et al. 2006). The general picture emerging from these surveys is that dwarf galaxies exhibit a wide range of morphology, from early-type to late-type and even irregular morphology. The ISM of these dwarf galaxies tends to be metal-poor, with low interstellar pressure and low dust-to-gas mass ratios (see review by C. Henkel, L. K. Hunt & Y. I. Izotov 2022). Due to their low-metallicities and ongoing star formation, dwarf galaxies are also believed to be ideal laboratories for studying star formation in conditions similar to the early Universe, potentially serving as low-redshift analogues to the high-redshift low-metallicity galaxies (e.g. N. Kumari et al. 2019; M. Mezcua, H. Suh & F. Civano 2019).

The properties of the dwarf galaxies mentioned above are, however, studied in high-density environments which might not be representative of the broader dwarf galaxy population in the Universe. This is because dwarfs in high-density environments or nearby massive galaxies have a high probability of interactions throughout their lifetime and therefore, the host galaxy's star formation will have a high environmental dependence. In contrast, a dwarf galaxy in a low-density or 'field' environment might experience fewer interactions and therefore might exhibit a different star formation history or metallicity compared to a typical dwarf in a high-density environment (e.g. G. Martin et al. 2021). For example, in the massive galaxy regime, Y.-j. Peng & R. Maiolino (2014) showed that the lack of interactions could result in higher metallicity, especially in field galaxies. In fact, the majority of dwarf galaxies are found in low-density, or 'field' environments (e.g. N. A. Bahcall et al. 1999; A. Dekel & J. P. Ostriker 1999; E. Tempel, E. Tago & L. J. Liivamägi 2012) where galaxy interactions are limited, allowing for a more secular evolutionary path (e.g. G. Martin et al. 2018; R. A. Jackson et al. 2020; G. Martin et al. 2021).

Studying dwarf galaxies in low-density environments requires a survey that has both a wide area as well as sufficient depth to detect targets with low surface brightness. Large-scale surveys such as the Sloan Digital Sky Survey (SDSS; e.g. K. Abazajian et al. 2003) have been successful in detecting dwarf galaxies in such low-density environments (e.g. S. D. Bykov, M. R. Gilfanov & R. A. Sunyaev 2024). However, SDSS is a magnitude-limited survey and is likely biased against detecting the general population of low surface brightness galaxies. Therefore, SDSS might largely capture the most actively star-forming dwarf galaxies (e.g. S. Kaviraj et al. 2025). This bias is also confirmed in the spatially resolved follow-up of dwarf galaxies via MANGA survey (Mapping Nearby Galaxies at APO; e.g. K. Bundy et al. 2015), who found that the majority of MANGA dwarf galaxies were star-forming late-type galaxies and that they had significantly lower metallicities compared to massive galaxies (see also J. Lequeux et al. 1979; C. A. Tremonti et al. 2004).

Surveys targeting deep fields, such as the Cosmic Evolution Survey (COSMOS; see N. Scoville et al. 2007) offer both the depth as well as wide area to detect a representative sample of dwarf galaxies in low-density environments. The ancillary multiwavelength coverage of the COSMOS field has enabled accurate characterization of sources within this field, including dwarf galaxies, such as star formation histories, SFR, stellar mass (M_*), morphological information etc. Recently, a sub-area of the COSMOS field was followed-up with *James Webb Space Telescope* (*JWST*) imaging via the COSMOS-Web survey (e.g. C. M. Casey et al. 2023). In this paper, we focus on multiwavelength morphological characterization of dwarf galaxies using imaging observations from the near-infrared camera (NIRCam) and the mid-infrared instrument (MIRI) in a sub-set of dwarf galaxies in COSMOS-Web at $z < 0.08$. Morphology is one of the fundamental properties of a galaxy and is believed to strongly relate to the formation history of a galaxy (see C. J. Conselice 2014). Morphological studies of dwarf galaxies have been conducted before where multiple mixes of morphological types are observed, beyond the classifications typically seen in the massive galaxy regime (e.g. G. Reaves 1983; A. Sandage & B. Binggeli 1984). However, as mentioned above, the vast majority of these studies target very nearby dwarfs or BCDs (e.g. H.-H. Loose & T. X. Thuan 1986; D. Kunth, S. Maurogordato & L. Vigroux 1988; S. van den Bergh 1998) and are usually limited to specific wavelength range, mostly optical.

In this paper, we select our parent sample from the low-density COSMOS field, particularly the targets in I. Lazar et al. (2024a). By combining observations across a wide range of wavelengths via *Hubble Space Telescope* (*HST*) and *JWST* imaging, we are able to assess the contribution of emission from dust and polycyclic aromatic hydrocarbons (PAHs) in the spectral energy distribution (SED) of the selected sources towards near- and mid-infrared wavelengths. We also compare the observed MIRI fluxes with predicted fluxes from TNG50 suite of simulations (D. Nelson et al. 2019) to infer if the star formation and ISM physics, along with feedback from star formation and/or black holes in TNG50 are sufficient to reproduce the MIR properties of these dwarfs.

This paper is organized as follows: in Section 2, we describe the selection of the sub-sample of dwarf galaxies from COSMOS-Web. In Section 3, we briefly present the *JWST* and MIRI imaging

observations and other ancillary data such as *HST*/ACS imaging used for the analysis in this paper. In Section 4, we present the analysis and results: specifically the comparison of the observed fluxes with predicted fluxes from TNG50 simulations, non-parametric morphological characterization using CAS (concentration, asymmetry, smoothness) parameters and morphological *k*-corrections. This is followed by the discussion of results in Section 5 and summary and conclusions in Section 6.

The following cosmological parameters are used throughout this paper: $H_0 = 70$ km s^{-1}, $\Omega_M = 0.3$ and $\Omega_\Lambda = 0.7$. North is up and East is to left in all the maps presented in this paper.

2 DWARF GALAXIES IN THE COSMOS SURVEY

The parent sample of dwarf galaxies has been obtained from the COSMOS2020 catalogue (see J. R. Weaver et al. 2022). The COSMOS field has ancillary photometric data across a wide range of wavelengths, from the ultraviolet (UV) through mid-infrared wavelengths using the following instruments: Galaxy Evolution explorer (GALEX; see M. A. Zamojski et al. 2007), MegaCam at the Canadian France Hawaii Telescope (CFHT; see M. Sawicki et al. 2019), the Advanced Camera for Surveys at the *Hubble Space Telescope* (*HST*/ACS; A. M. Koekemoer et al. 2007), Hyper-Suprime Cam (HSC; see H. Aihara et al. 2018) and Suprime-Cam (Y. Taniguchi et al. 2015) at Subaru Telescope, VISTA InfraRed CAMera (VIRCAM) at the Visible and Infrared Survey Telescope for Astronomy (VISTA; see H. J. McCracken et al. 2012) and the Infrared Array Camera (IRAC) aboard the *Spitzer* telescope (see M. L. N. Ashby et al. 2018). The multiwavelength photometry has resulted in an accurate derivation of several host galaxy parameters such as redshift (z), stellar mass (M_*), and star formation rates (SFR) for ∼1.7 million sources in the COSMOS field. Further details about the COSMOS2020 catalogue are available in J. R. Weaver et al. (2022).

Recently, I. Lazar et al. (2024a) performed a systematic morphological characterization of dwarf galaxies in the COSMOS2020 catalogue using optical *gri* colour composite images from the Hyper Suprime-Cam Subaru Strategic Program (HSC-SSP) ultradeep layer (e.g. H. Aihara et al. 2018, 2019). The HSC imaging has the advantage that it is ∼5 mag deeper than the standard depth SDSS imaging and ∼10 mag deeper than the detection limit of the SDSS spectroscopic main galaxy sample. I. Lazar et al. (2024a) used a sub-sample of 257 dwarf galaxies, which have a stellar mass range of $10^8 < M_* < 10^9$ M$_\odot$, and $z < 0.08$. The $z < 0.08$ target selection ensured sufficient spatial resolution to morphologically characterize these galaxies. Given the completeness of the COSMOS2020 catalogue for galaxies with $M_* > 10^8$ M$_\odot$ out to $z \sim 0.3$, the 257 dwarf galaxies present an unbiased, statistical and a representative benchmark sample of nearby dwarfs in low-density environments.

We briefly describe the results in I. Lazar et al. (2024a) and refer to reader to the paper for further details. 90 per cent of the dwarf galaxies exhibit the canonical early-type and late-type morphology that are also observed in massive galaxies. Additionally, 10 per cent of the dwarf galaxies also exhibit 'featureless' morphological class [also referred to as dwarf spheroidals in J. Kormendy & L. C. Ho (2013)] characterized by a lack of both central light concentration (that is seen in early-types) and any structure indicative of a disc. The featureless class is not observed in the massive galaxy regime. Additionally, the structural and photometric properties of the dwarf and massive early-type galaxies diverge significantly, which suggests different formation channels of the two classes. While massive early-types and late-types are predominantly red and blue respectively, dwarf early-types and late-types share similar colour distributions. Finally, while massive early-types typically exhibit negative/flat colour gradients, dwarf early-types show positive colour gradients with ∼50 per cent of dwarf early-types showing prominent blue cores extending to ∼1.5 R$_e$ (e.g. I. Lazar et al. 2024b). This may suggest that the general population of dwarf galaxies may still have ongoing star formation and that their ISM may consist of significant amounts of dust and gas enriched with chemical elements.

Given a detailed morphological characterization, coupled with multiwavelength photometric information from the COSMOS2020 catalogue, we derive the parent sample of dwarf galaxies from the 257 targets in I. Lazar et al. (2024a). Specifically, we search for the dwarf galaxies that are covered as a part of the near-infrared and mid-infrared imaging campaign from COSMOS-Web (see C. M. Casey et al. 2023) to characterize the warm and hot dust properties of the dwarf galaxies and compare this with archival rest-frame optical images from the *HST*. The *JWST* and *HST* imaging observations and data are presented in the following section.

3 JWST AND HST OBSERVATIONS

The COSMOS field has been observed with high-resolution imaging with *HST* and *JWST*. Here, we briefly describe these observations and the dwarf galaxy sample that are covered as a part of these surveys.

3.1 *JWST*/NIRCam and MIRI imaging

COSMOS-Web survey is a *JWST* Cycle-1 treasury programme (GO-1727, PI: Kartaltepe & Casey; see C. M. Casey et al. 2023) that covered 0.54 deg^2 of the COSMOS survey (e.g. N. Scoville et al. 2007) with four filters of the NIRCam (*F*115*W*, *F*150*W*, *F*277*W*, *F*444*W*; see M. J. Rieke et al. 2023) and 0.19 deg^2 of the COSMOS survey with the *F*770*W* filter of the MIRI (A. Glasse et al. 2015; G. S. Wright et al. 2023). Here, we present a brief overview of the COSMOS-Web observations and refer the reader to C. M. Casey et al. (2023) for further details.

The COSMOS-Web images were obtained in multiple visits between January 2023–January 2024, with a total exposure time of ∼255 h split between the NIRCam and MIRI observations. The data are reduced with the *JWST* calibration pipeline (see H. Bushouse et al. 2023) with further customized steps, which are elaborated in M. Franco et al. (2025) and S. Harish et al. (2025). The final reduced NIRCam and MIRI images from the COSMOS-Web have a spatial sampling of 60 mas pixel^{-1}. For NIRCam, a finer sampling of 30 mas pixel^{-1} is available, however, we use the 60 mas pixel^{-1} sampling to compare with the MIRI images. Astrometric accuracy for both NIRCam and MIRI imaging was ensured through customized procedures detailed in M. Franco et al. (2025) and S. Harish et al. (2025), respectively. For the NIRCam data, we employed the external *JWST*/*HST* alignment tool (JHAT; see A. Rest et al. 2023), which provides improved precision compared to the current *JWST* pipeline adjustments. For the MIRI data, the astrometry was refined by cross-matching the MIRI source catalogue with a reference catalogue constructed from the COSMOS2020 survey. The NIRCam and MIRI images reach a 5σ point-source depth of ∼27.5–28.2 mag and ∼25.3–26.0 mag, respectively. The depth of a particular pointing depends on the number of exposures at that location in the NIRCam and/or

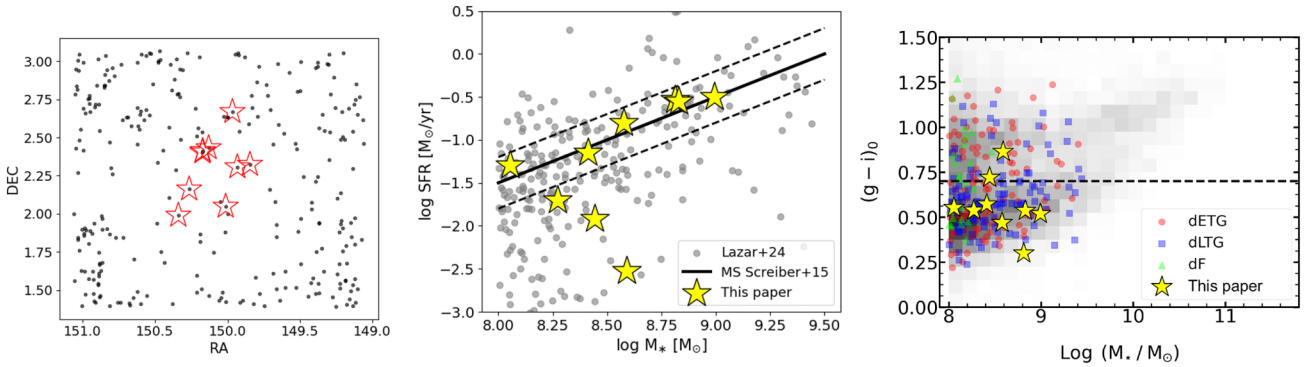

Figure 1. The *left panel* shows the spatial distribution of the parent sample of dwarf galaxies in the COSMOS field from I. Lazar et al. (2024a). The sources highlighted by red stars are covered by NIRCam and MIRI imaging campaigns of the COSMOS-Web survey. The *middle panel* shows the location of the dwarf galaxies covered in the COSMOS-Web campaign, compared to the parent I. Lazar et al. (2024a) sample. Most of the dwarf galaxies are located on the main sequence of massive star-forming galaxies (solid line with ±0.3 dex regions shown by dashed line, see C. Schreiber et al. 2015), extrapolated to lower masses. Three galaxies are below the main sequence in the passive galaxy regime. The *right panel* shows the location of the dwarf galaxies in the colour $(g-i)_0$ versus M_* plane. The grey colour-scale background shows the location of all galaxies from the COSMOS survey (including massive galaxies) and the coloured data points show the different morphological types of dwarf galaxies from I. Lazar et al. (2024a). The dotted line demarcates blue (bottom half) and red (top half) galaxies. The sample presented in this paper, shown as yellow stars show both red and blue dwarfs are detected with the COSMOS-Web imaging campaigns.

MIRI mosaic. The depth from *JWST* imaging campaign of the COSMOS survey is at least 1–3 mag deeper than the *HST*/ACS *I*-band images (see N. Scoville et al. 2007).

We searched for available COSMOS-Web NIRCam and MIRI imaging coverage of the 257 dwarf galaxies from I. Lazar et al. (2024a). Unlike the NIRCam mosaic, the MIRI footprint in the COSMOS-Web survey is not contiguous, but rather it is distributed into 152 distinct regions, each region covering 4.2 × 4.2 arcmin^2, corresponding to the MIRI field of view. The distribution of all the 257 dwarfs in the RA–Dec. plane is shown as black circles in Fig. 1. Targets covered by both NIRCam and MIRI observations are highlighted as red stars. Out of the 257 dwarf galaxies in I. Lazar et al. (2024a), we find nine galaxies that are covered by the NIRCam and MIRI imaging campaigns, which are the focus of this paper. The basic properties of these nine dwarf galaxies are reported in Table 1. For NIRCam, we use the *F*277*W* filter ($\lambda_{\rm pivot} = 2.776$ µm, bandwidth $= 0.672$ µm) for the analysis presented in this paper, as *F*277*W* offers the highest depth compared to the other filters and has comparable spatial resolution between the different filters. For MIRI, we use the default *F*770*W* filter ($\lambda_{\rm pivot} = 7.639$ µm, bandwidth $= 1.95$ µm)

The selected dwarf galaxies are in the redshift range $z \sim 0.02-0.08$, have a stellar mass $M_* \sim 1.1-10 \times 10^8$ M$_\odot$ and SFR in the range 0.003−0.3 M$_\odot$ yr^{-1}. The SFRs and M_* values place these dwarf galaxies on or below the main sequence of massive star-forming galaxies (extrapolated to lower masses), as shown in the middle panel in Fig. 1. This is also reflected in the colour-mix of the dwarf galaxies: their rest-frame $(g-i)_0$ values are in the range 0.3−0.9. The right panel in Fig. 1 shows the distribution of the selected dwarf galaxies in the $(g-i)_0$ versus M_* space. The morphology of these dwarfs, as determined via deep HSC imaging in I. Lazar et al. (2024a), are roughly evenly split between early-type and late-type. The selection of both star forming and passive, blue and some red dwarfs, along with the equal split in the morphology of the sample suggests that the selected dwarf galaxies for this paper are nearly representative of the overall dwarf population within the stellar mass range 10^8-10^9 M$_\odot$.

3.2 *HST*/ACS imaging

In addition to the NIRCam and MIRI imaging, we also searched for publicly available archival *HST*/ACS images as a part of the COSMOS-*HST* campaign (see A. M. Koekemoer et al. 2007; N. Scoville et al. 2007). The ACS data of the COSMOS field were taken with the *F*814*W* filter (*I* band, $\lambda_0 = 8333$ Å, bandwidth $= 2511$ Å) for an area of 1.64 deg^2. The final reduced images have a spatial sampling of 30 mas pixel^{-1}, with an average PSF (full width at half-maximum, FWHM) of 0.1 arcsec. The *HST* images were rebinned to a pixel scale of 60 mas to be consistent with the NIRCam and MIRI images. All the nine dwarf galaxies with the NIRCam and MIRI coverage presented in Section 3.1 have publicly available *HST*/ACS imaging as well.

The *HST*/ACS, NIRCam and MIRI images of three of the dwarf galaxies (IDs: 5, 120 and 232) are shown as examples in Fig. 2. Plots for the rest of the targets are moved to the Appendix A.

4 ANALYSIS AND RESULTS

The primary goals of this paper are to draw inferences on the characteristics of the ISM of these dwarfs i.e. whether we expect the dwarfs to exhibit the level of mid-infrared emission as observed in the MIRI images and estimate the change in the morphological characteristics of the dwarf galaxies with wavelength i.e. from optical (*HST*) to near-infrared (NIRCam) and mid-infrared (MIRI).

To analyse the *HST* and *JWST* images described in Section 3, we first extract rectangular cut-outs from the respective image mosaics. The cut-outs have an area of $\sim 15 \times 15$ arcsec^2, which roughly cover the spatial extent of the dwarf galaxies. Depending on the redshift of the targets, this covers a physical scale of $\sim \mathbf{7} \times \mathbf{7}$ to $\sim \mathbf{22} \times \mathbf{22}$ kpc^2. The spatial resolutions of the ACS/*F*814*W*, NIRCam/*F*277*W* and MIRI/*F*770*W* are ∼0.1, 0.1, and 0.28 arcsec, respectively. Clearly, the *HST* and NIRCam images offer nearly 3 times better spatial resolution than the MIRI images. The images shown in Fig. 2 (and Figs A1 and A2) show the true resolution of the final reduced images. However, for

Table 1. Basic properties of the dwarf sample presented in this paper. (a) Target IDs correspond to the catalogue published in I. Lazar et al. (2024a), (b) and (c) report the coordinates of the target, (d) reports the redshift, (e) and (f) report the star formation rate and stellar mass calculated from the ancillary multiwavelength data and presented in the COSMOS2020 catalogue (see J. R. Weaver et al. 2022). Finally, (g) and (h) report the colour and morphological type of the dwarf galaxies, as calculated in I. Lazar et al. (2024a) using HSC imaging campaign.

Target ID	RA	Dec.	z	log SFR	log M_*	$(g-i)_0$	Morphology
	J2000	J2000		$M_\odot\ yr^{-1}$	$M_\odot$		
(a)	(b)	(c)	(d)	(e)	(f)	(g)	(h)
5	10:00:41.546	+02:24:15.080	0.0219	−1.92	8.44	0.721	E
61	10:00:41.073	+02:24:46.760	0.0522	−1.70	8.27	0.538	S
72	09:59:43.716	+02:18:24.630	0.0582	−1.30	8.05	0.553	S
104	10:01:21.578	+01:59:21.820	0.0632	−0.80	8.57	0.469	S0
120	10:01:03.608	+02:09:40.780	0.0637	−0.54	8.81	0.300	S
132	09:59:51.921	+02:40:07.180	0.0643	−0.55	8.83	0.536	E
175	09:59:22.925	+02:19:22.960	0.0683	−1.15	8.41	0.572	E
232	10:00:31.370	+02:25:53.010	0.0732	−0.50	8.99	0.520	S
269	10:00:03.070	+02:02:54.370	0.0782	−2.52	8.59	0.864	E

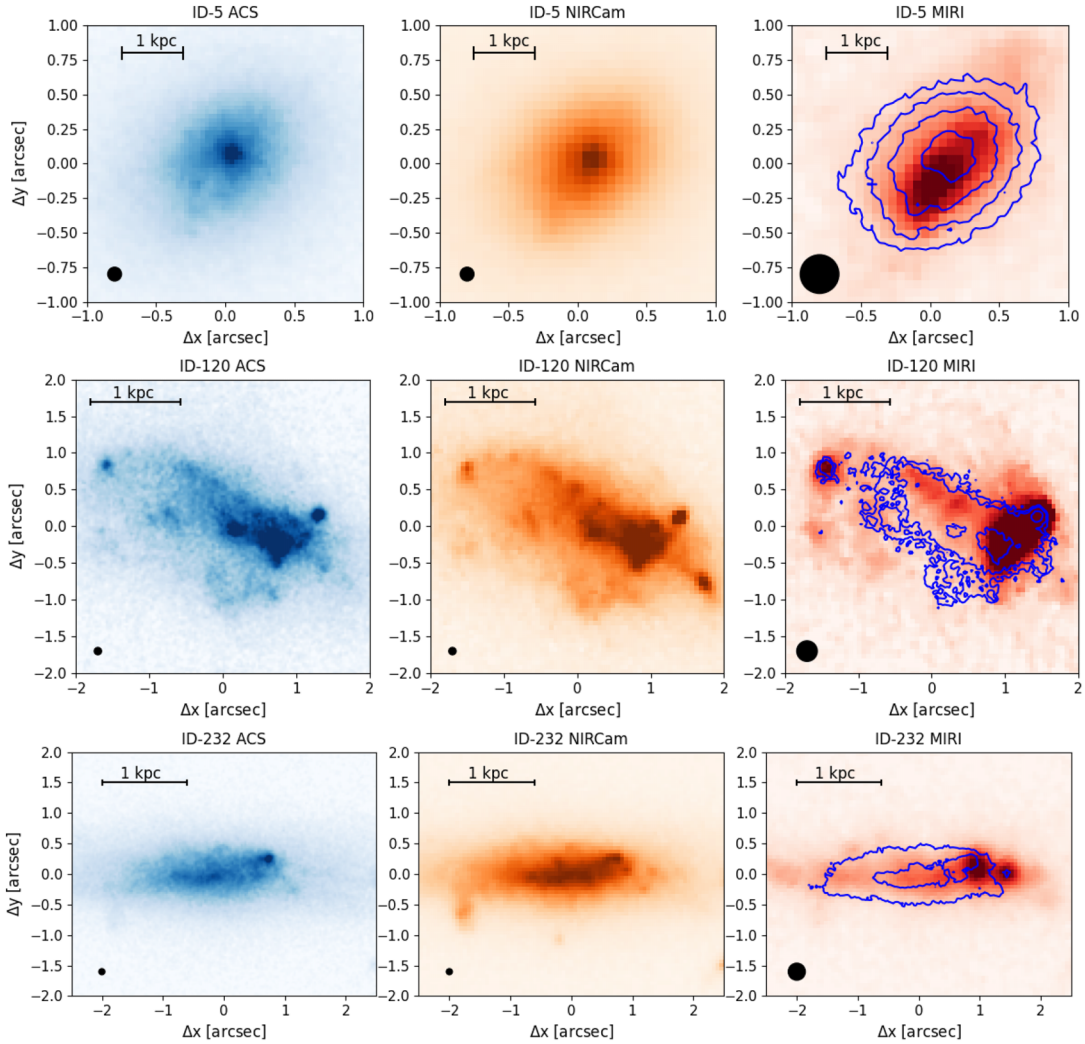

Figure 2. The left, middle, and right panels show the *HST*/ACS *F*814*W*, *JWST*/NIRCam *F*277*W* and *JWST*/MIRI *F*770*W* images of three of the dwarf galaxies (from top to bottom: IDs 5, 120, and 232) presented in this paper. The contours on the MIRI images in the right panel represent the *F*814*W* emission from the *HST*/ACS images in the left panel. The horizontal bar shows the physical 1 kpc scale and the circle in the bottom left shows the PSF (FWHM) of the respective images. The potential emission from the dust becomes clearly visible in the MIRI images, which are otherwise absent in the *HST* images. See Section 4.1 for further details.

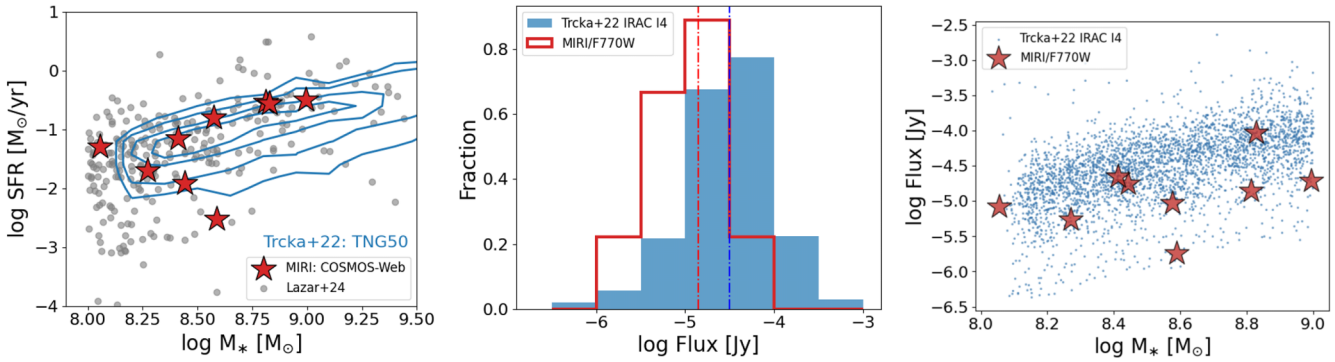

Figure 3. The *left panel* shows the location of the TNG50 galaxies (contours), along with the parent dwarf galaxy sample (circles), and the sample presented in this paper (stars) in the SFR–M_* plane. The *middle panel* shows the flux distributions of the mock IRAC-I4 flux from A. Trčka et al. (2022) (filled histogram) and the observed MIRI/*F770W* fluxes in this paper (histogram outline). The *right panel* shows the fluxes in the middle panel as a function of stellar mass for TNG50 galaxies (circles) and the sample presented in this paper (stars). Further details about the comparison between TNG50 data and MIRI observations are given in Section 4.1.

comparative morphological characterization, presented in this section, it is important to analyse images that have similar spatial resolution. As MIRI imaging has the worst spatial resolution, we convolve the NIRCam and ACS images with a Gaussian kernel to match them to the resolution of the MIRI images.

4.1 NIRCam and MIRI detection rates of dwarf galaxies

We begin by discussing the detection rates of dwarf galaxies in the near- and mid-infrared wavelengths. All nine galaxies are detected in NIRCam and MIRI imaging from the COSMOS-Web survey, resulting in a 100 per cent detection rate. Given the shallow gravitational potential wells of dwarf galaxies, this raises important questions about their ISM content and composition, as well as the effectiveness of stellar and AGN feedback in expelling gas and dust from their ISM. The observed 100 per cent detection rate in both wavelength ranges suggests that dwarf galaxies largely retain some of their ISM, potentially in terms of their warm gas and dust content, including PAHs.

We verify if the observed fluxes in the NIRCam and MIRI images are consistent with expectations from the fluxes of low-mass galaxies in the TNG50 simulation (e.g. D. Nelson et al. 2019; A. Pillepich et al. 2019). TNG50 simulates the evolution of a ∼50 Mpc^3 box from cosmological initial conditions to $z = 0$ using the moving-mesh code AREPO (e.g. V. Springel 2010; R. Weinberger, V. Springel & R. Pakmor 2020). TNG50 has the highest resolution within the IllustrisTNG suite of simulations (e.g. F. Marinacci et al. 2018; J. P. Naiman et al. 2018; V. Springel et al. 2018). We compare our observed MIRI flux with mock IRAC I4 flux from A. Trčka et al. (2022), who implemented the radiative transfer (RT) code, Stellar Kinematics Including Radiative Transfer (SKIRT; e.g. M. Baes et al. 2011; P. Camps & M. Baes 2015) on ∼14 000 $z \leq 0.1$ galaxies drawn from the TNG50 simulation. The RT implementation in A. Trčka et al. (2022) modelled light from evolved stars, star-forming regions and the diffuse dust. Emission from stars was modelled for star particles with ages above 10 Myr using G. Bruzual & S. Charlot (2003) stellar population synthesis models, with a Chabrier initial mass function (G. Chabrier 2003). Young star-forming regions were modelled with MAPPINGS-III SED templates (B. Groves et al. 2008), including a photodissociation region with a covering fraction. The diffuse dust was modelled only in relatively dense and cold gas cells according to the boundary condition criteria in P. Torrey et al. (2012, 2019). Following detailed calibration by A. Trčka et al. (2022), a fixed dust-to-metal mass ratio of 20 per cent was assumed. The dust grain distribution was modelled with the The Heterogeneous dust Evolution Model for Interstellar Solids (THEMIS) dust models (A. P. Jones et al. 2017) using 15 grain size bins. Further details of the RT implementation are available in A. Trčka et al. (2022).

Forward-modelled fluxes in A. Trčka et al. (2022) are available for several broad-band filters from UV to sub-mm wavelengths. For the purpose of this paper, we choose the mock IRAC I4 fluxes, as the MIRI/*F770W* filter used in this paper is the closest match to the IRAC-I4 band ($\lambda_0^{\rm IRAC-I4} \sim 7.8\,\mu$m). We use the SNAPSHOT_91 data, corresponding to a redshift of $z \sim 0.1$, which is also closest to the median redshift ($z \sim 0.08$) of the observed dwarf sample presented in this paper. Fig. 3 shows the comparison between the observed dwarf sample presented here and the TNG50 sample. The parent dwarf galaxy sample (grey circles) and the sample selected here (red stars) lie within the area occupied by the TNG50 galaxies (blue contours) in the SFR–M_* plane at $\log M_*/\,{\rm M}_\odot < 9$, as shown in the left panel in Fig. 3. This further confirms the representative nature of the dwarf galaxies selected in this paper. The middle panel in Fig. 3 shows the mid-infrared flux distributions of the observed MIRI sample (red histogram) and the IRAC-I4 TNG50 sample (blue histogram). The median values of the flux distributions are within 0.5 dex of each other, as apparent from the vertical red and blue lines in the middle panel in Fig. 3. We performed a Kolmogorov–Smirnov (KS) test (J. L. Hodges 1958) to test whether the underlying observed and simulated flux distributions are different. For a null hypothesis that the samples are drawn from two different distributions, the KS test yields a p-value of 0.4, which is insignificant at the standard 5 per cent level. Therefore, we conclude that the observed and the simulated flux distributions are similar. In other words, the simulated TNG50 mid-infrared fluxes are in agreement with the observed mid-infrared fluxes from MIRI. The quoted significance levels come with a few caveats. First, the computed p-value is sensitive to the choice of binning in the histogram, which we set according to the maximum uncertainty expected in flux values (∼ 0.5 dex) in both the simulated and observed data. In addition, the significance is influenced by the limited number of observed galaxies (<10), sharply in contrast to the much larger simulated sample (≈14 000), leading to low-number statistical effects on the observational side. Lastly, the

right panel in Fig. 3 shows the mid-infrared flux as a function of stellar mass for the MIRI (red stars) and TNG50 (blue circles) sample. We do not see any systematic offsets between the observed and simulated fluxes with mass. This suggests again that the simulations are roughly in agreement with the observations for the mass range probed in this paper. We discuss this comparison between observations and simulations further in Section 5.

4.2 Multiwavelength morphological characterization

4.2.1 Visual characterization

Fig. 2 shows the *HST*/*F*814*W* (*I* band, left panel), NIRCam/*F*277*W* (middle panel), and MIRI/*F*770*W* (right panel) images of three dwarf galaxies presented in this paper, as examples. Plots for the rest of the sample are moved to the Appendix A (Figs A1 and A2). The blue contours on the MIRI images (right panel in these figures) show the *HST*/*F*814*W* emission shown in the left panels. From these images, it is clear that the nine dwarf galaxies detected with *JWST* imaging have a wide range of morphology: from early-type to late-type, including mergers. In this section, we discuss the morphological characteristics of these dwarf galaxies.

Based on visual classification, the MIRI detected sample is evenly split between early-types and late-types, indicating that dwarf early-types retain some of their ISM like their late-type counterparts. The distribution of the dwarfs into these two categories is consistent with the rest-frame $(g-i)_0$ colours of the dwarf galaxies reported in I. Lazar et al. (2024a). In fact, looking at the colour distribution of the nine dwarf galaxies (see right panel in Fig. 1), two of the dwarf galaxies show red colours. This corresponds to ≈20 per cent red fraction, although these are low number statistics. The observed red fraction in *JWST* sources is consistent with the red fraction in the parent population of dwarf galaxies (13–40 per cent; I. Lazar et al. 2024a), albeit this number has large uncertainties. We find two interacting dwarfs in our sample (ID-072 and ID-120) i.e. 20 per cent of the sample, which is within the range found in the parent sample of dwarf galaxies in I. Lazar et al. (2024a).

In summary, despite the low number statistics presented due to the coverage of MIRI imaging, based on the visual classifications and the colour distribution of dwarf galaxies in our sample, our results suggest that the MIRI detections are not strongly biased towards a particular class or colour of dwarf galaxies. The selected dwarfs span a wide range of the SFR–M_* plane, as shown in Fig. 3, which suggests that the sub-sample of dwarf galaxies presented here is representative of larger dwarf population in low-density environments.

Although the morphological classification itself does not change as a function of the wavelength, there are subtle differences that may suggest the presence of dust lanes or dust clumps and regions subjected to dust obscuration in these galaxies. For example, in ID-5 (top panel in Fig. 2), the *HST* image shows a lack of emission towards the South-East of the nucleus. The MIRI image, on the other hand, shows enhanced emission in this region, suggesting that the rest-frame optical emission is possibly obscured by a dust lane, as seen in the Milky Way as well as many nearby massive galaxies (e.g. NGC 7172). The dust lanes observed in early-type galaxies like ID-5 may also point to past merger activity in these dwarf systems (e.g. S. Kaviraj et al. 2012). Evidence of dust clumps is also seen in ID-120, where the MIRI image reveals excess mid-infrared emission towards the western regions of the galaxy, in contrast to the lack of corresponding emission in the *HST* and NIRCam images.

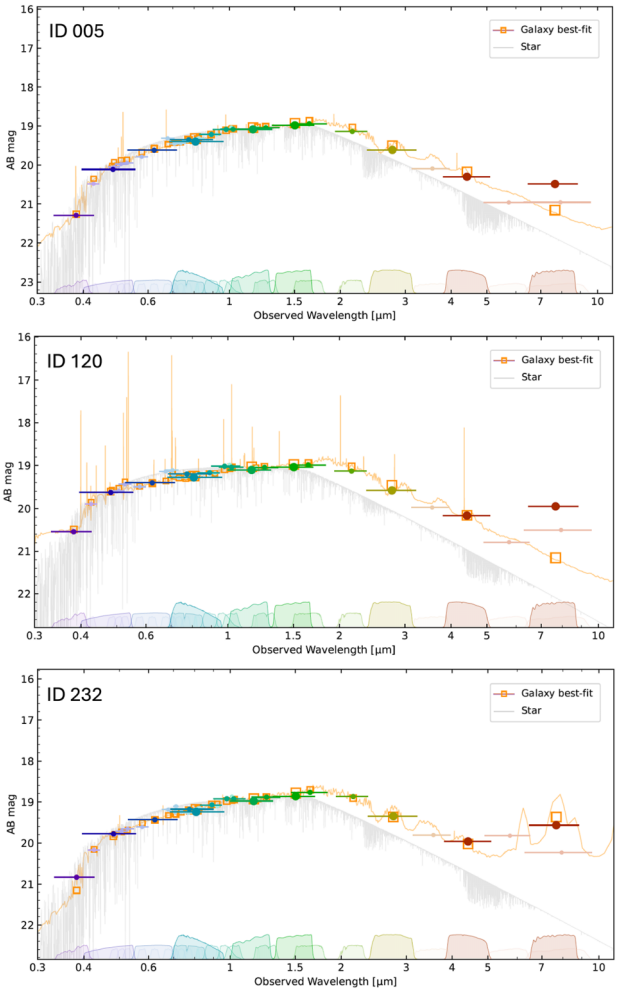

Figure 4. SED fits of targets ID-5 (top panel) and ID-120 (middle panel), and ID232 (bottom panel) using PROSPECTOR. The coloured circles show the different photometric data points from COSMOS2025 (M. Shuntov et al. 2025) corresponding to the following instruments and filters: HSC (g, r, i, z, y), UVISTA (Y, J, H, K), IRAC (1, 3, 4), *HST* (F814W), NIRCam (*F*115*W*, *F*150*W*, *F*277*W*, *F*444*W*) and MIRI (*F*770*W*). The orange curve shows the best-fitting SED model. In all the targets, contribution from small and large dust grains and PAHs becomes apparent at mid-infrared wavelengths, the excess emission above stellar model (blackbody fit shown in grey colour). This is further reinforced by the multiwavelength visual analysis of these targets, that already indicated possible presence of dust lanes and dust clumps.

We also obtained SED fits from the COSMOS-Web survey, as described in M. Shuntov et al. (2025). To validate these results, we performed independent SED fitting using the PYTHON-based PROSPECTOR code (see B. D. Johnson et al. 2021; B. Bichang'a et al. 2024), which are consistent with the SED fits in M. Shuntov et al. (2025). Fig. 4 presents example SED fits for ID-5, ID-120, and ID-175 in the top, middle, and bottom panels, respectively. The SED fits for the rest of the sample presented in this paper are shown in Fig. A3. The fits clearly show a substantial contribution from dust grains and PAHs in the mid-infrared, beyond the stellar component, which is represented by the grey blackbody model in Fig. 4. For the galaxies presented in this paper,

Table 2. Parametric and non-parametric morphological analysis of the dwarf galaxies presented in this paper. The table compares the Sérsic index (n) and 'CAS' parameters (C = Concentration, A = Asymmetry, S = Clumpiness) from HSC/I band (I. Lazar et al. 2024a) and *HST*/I band images shown in Figs 2, A1 and A2. See Section 4 for further details.

ID	HSC				*HST*			
	n	C	A	S	n	C	A	S
5	1.7	2.96	0.03	−0.001	1.0	2.90	0.03	0.004
61	1.4	3.07	0.14	0.02	1.0	2.54	−0.02	-0.03
72	0.7	2.54	0.24	0.03	0.6	2.22	0.23	0.02
104	1.9	3.34	0.03	0.00	1.1	2.92	0.03	0.01
120	0.8	2.89	0.20	0.04	0.7	2.26	0.30	0.02
132	1.9	3.09	0.06	0.085	1.1	2.86	0.09	0.004
175	1.2	2.83	0.02	0.08	0.9	2.74	0.02	0.02
232	1.1	2.69	0.10	0.04	0.8	2.66	0.11	0.02
269	2.0	3.10	0.01	0.05	1.2	3.07	0.03	-0.003

we estimate that stellar emission contributes anywhere between about 6-70 per cent of the rest-frame $\sim 7\mu$m flux, with a median of 45 per cent, indicating that for most sources, more than half of the mid-infrared emission arises from warm or hot dust and PAH features. The exact nature of the emission at mid-infrared wavelengths can be verified with dedicated spectroscopic follow-up with the medium resolution spectrograph (MRS) of MIRI. The implications of these dust features, including comparison with studies in the massive galaxy regime are further discussed in Section 5.

4.2.2 *Parametric and non-parametric morphological characterization*

In addition to the visual classification done above, parametric and non-parametric methods can be employed to quantify the morphological characteristics of the dwarf galaxies detected in different wave bands. Parametric methods such as fitting the galaxy surface brightness with Sérsic profile are useful to estimate the Sérsic index, which can then be compared against different classes (early-types or late-types) and also can be compared against the values observed in the massive galaxy regime. We have used the STATMORPH package to derive Sérsic parameters using two-dimensional single-component Sérsic profile fits using PYTHONASTROPY modelling package within STATMORPH. Further details on Sérsic fits are available in V. Rodriguez-Gomez et al. (2019) and I. Lazar et al. (2024a). The distribution of Sérsic indices in the parent dwarf early-type galaxies (ETG) and late-type galaxies (LTG) from I. Lazar et al. (2024a) show overlapping values with the median Sérsic index of 1.5 in dwarf ETG and 1.3 in dwarf LTG. The Sérsic indices calculated from imaging using space telescopes are even lower than that of the parent dwarf galaxies. This is clear from the values quoted in Tables 2 and A1. The average Sérsic index for dwarf early-types from HSC/I band is 1.7, compared to 1.1 with *HST*/I band. Similarly, the average Sérsic index for dwarf late-types from HSC/I band is 1.0, compared to 0.8 with *HST*/I band. Therefore, for the same waveband, ground-based imaging results in higher Sérsic indices, compared to space telescope imaging. This may be due to larger PSFs in ground-based images and/or the detection or more diffuse emission sensitive in ground-based HSC observations, which are deeper than the *HST* imaging. Furthermore, the Sérsic indices appear to decrease as a function of wavelength, at least for the dwarf ETGs (1.1 to 0.9 from *HST* to MIRI imaging), while it is nearly constant for dwarf late-type galaxies. The difference in Sérsic indices observed in dwarf galaxies is less stark when compared to ETGs and LTGs in massive galaxies, where the corresponding Sérsic indices are 3.5 and 1.5, respectively (see also S. M. Faber & D. N. C. Lin 1983).

Non-parametric methods, on the other hand, do not require fitting the surface brightness profiles with a known function. For example, studies by C. J. Conselice (2003), R. G. Abraham, S. van den Bergh & P. Nair (2003), and J. M. Lotz, J. Primack & P. Madau (2004) introduced morphological parameters such as concentration (C), asymmetry (A), clumpiness (S), M_{20}, and the Gini coefficient. We refer the reader to the references (see also I. Lazar et al. 2024a) for the definitions of each of these parameters. The former three are collectively known as 'CAS' parameters. In the nearby Universe, such non-parametric morphological characterization has suggested that massive ETGs show higher concentration, lower asymmetry, and lower clumpiness than their LTG counterparts. We aim to perform a similar analysis for our dwarf galaxy sample in different wavebands.

We refer the reader to I. Lazar et al. (2024a) for details regarding the derivation of CAS parameters. The process is briefly explained here. Before determining the CAS parameters, we masked external sources such as interlopers, foreground stars, and foreground or background galaxies that would otherwise have interfered with the surface brightness profile of the primary dwarf sources. The asymmetry, clumpiness, concentration, M_{20} and Gini coefficient were estimated using the STATMORPH package in PYTHON (see V. Rodriguez-Gomez et al. 2019). These parameters derived from the *HST* and *JWST* images, including ground-based HSC imaging are reported in Tables 2 and A1.

Similar to previous studies targeting well-resolved galaxies in the nearby Universe, we see that dwarf early-types exhibit a higher concentration, lower asymmetry, and lower clumpiness than their late-type counterparts across all the *HST*, NIRCam and MIRI images (see results from massive galaxies in C. J. Conselice 2003; B. W. Holwerda et al. 2014; T.-Y. Cheng et al. 2021). ID 120 shows visible signatures of interactions or mergers and as expected, it shows a higher value of asymmetry. We note that for ID-232, the asymmetry parameter in MIRI is nearly 3 times that of *HST* or NIRCam. This is because of the detection of additional (dust) clump towards the West of the galaxy, as shown in the bottom panel of Fig. 2. Therefore, general trends in the average CAS values agree well with the findings in the literature, regardless of the wavelength.

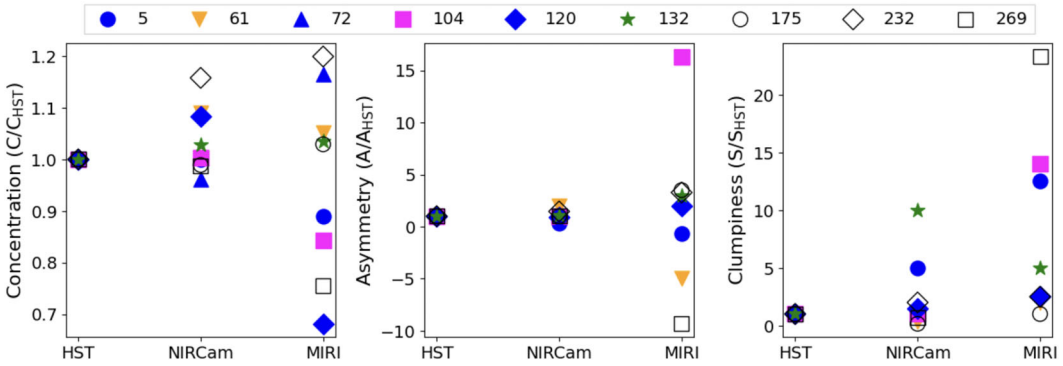

Figure 5. The *top panel* shows the concentration (C, left panel), asymmetry (A, middle panel), and clumpiness (S, right panel) as a function of the *HST*/*F*814*W*, NIRCam/*F*277*W*, and MIRI/*F*770*W* for the individual targets (different colours and symbols) presented in this paper. The values in each filter have been normalized to the *HST*/*F*814*W* to guide the change in the respective parameters.

We then compare the CAS parameters derived from HSC *I* band and *HST*/*F*814*W* images to assess how these measurements differ between lower-resolution ground-based imaging and the higher-resolution *HST* data. We choose *I* band (∼8300 Å) in both cases, to ensure there is no wavelength dependence introduced in the CAS parameters. Table 2 summarizes the CAS values obtained from HSC and *HST* images. Note that no PSF matching has been applied between the HSC (∼0.6 arcsec) and *HST* (∼0.09 arcsec) data sets. From the values in Table 2, we find that the concentration index (C) generally decreases from HSC to *HST* images, which is likely due to the narrower PSF of *HST*. The asymmetry (A) shows a slight increase in some galaxies, but remains broadly consistent across the two data sets. Similarly, clumpiness (S) is also largely consistent between HSC and *HST* images. Overall, the CAS parameters derived from ground-based and space-based imaging appear broadly consistent.

We then compared the morphological parameters from the HST, NIRCam, and MIRI images. However, before this comparison, we ensured that the images under analysis have the same spatial resolution. The MIRI images have 3 times worse spatial resolution (∼0.28 arcsec) compared to *HST* and NIRCam images (both ∼0.09 arcsec). Therefore, as mentioned earlier, the *HST* and NIRCam images were brought to the resolution of the MIRI images, by convolving them with a Gaussian kernel. Fig. 5 shows the CAS parameters as a function of wavelength (*HST* = 8333 Å, NIRCam ∼ 2.7 μm, and MIRI ∼ 7.7 μm) for each target. The CAS parameters in Fig. 5 have been normalized to the values of the *HST* images to better guide the relative changes in the parameters for each target. From this figure and from the values reported in Table A1, it is clear that the morphological parameters change as a function of wavelength. Generally, the CAS parameters appear to increase as a function of wavelength in absolute terms, with MIRI images show the maximum dispersion or range in the CAS parameters compared to NIRCam or *HST* images.

We calculate the differences in the individual parameters, namely, change in concentration (ΔC), asymmetry (ΔA), clumpiness (ΔS), M_{20} (ΔM_{20}), and Gini (ΔGini) for each target. These differences in the morphological parameters can also be visualised for individual targets via the plots in Figs 6 and 7. The top panels in Fig. 6 show ΔC (left panel), ΔA (middle panel), and ΔS (right panel) for different morphological types, classified visually (ETGs: E/S0 or LTGs: S). The lower panels in Fig. 6, on the other hand, show ΔC, ΔA, and ΔS as a function of stellar mass, M_*. Fig. 7 shows similar plots, but for M_{20} and Gini parameters. The data points in these plots are further separated into the difference in each band: blue shows *HST*−NIRCam, orange shows NIRCam−MIRI, and red shows *HST*−NIRCam. Only the absolute values in these changes are displayed in these plots.

On average, the morphological difference calculated from *HST*−NIRCam data sets show the least variation compared to NIRCam−MIRI, and *HST*−MIRI. This is clear from the dashed blue, orange, and red lines in Figs 6 and 7, which correspond to average values of the parameter differences. This is consistent with the trends observed in Fig. 5 and also while visually analysing images in Figs 2, A1, and A2. For example, in ID-232 in the bottom panel in Fig. 2, the clump towards the West edge of the galaxy is prominent in the MIRI image (right panel), but is otherwise absent in the *HST* and NIRCam images in the left and middle panels, respectively. The contrary is also true i.e, due to the depth of the NIRCam and *HST* images, some of the structures are more prominent or clearly visible in NIRCam and *HST* images instead. For example, the late-type morphology of ID-269 is evident in *HST* and NIRCam images in the bottom panel of Fig. A2. However, the MIRI image depth is not sufficient to detect the extended structure.

We do not find any trend between ΔC, ΔA, and ΔS with stellar mass. The M_{20} parameter is relatively stable with stellar mass, as evident from the right panel in Fig. 7. The lack of a clear trend with either morphological type or stellar mass may be due to the relatively narrow range in stellar mass probed in the dwarf galaxies presented here.

Fig. 8 shows the distribution of these morphological parameters in different parameter spaces, namely clumpiness versus asymmetry (left panel), asymmetry versus concentration (middle panel), and clumpiness versus concentration (right panel). These plots have usually been used to distinguish between early-type and late-type galaxies in the massive galaxy regime, however this may not be true in the dwarf regime (I. Lazar et al. 2024a). To visualize where the dwarf galaxies presented in this paper lie with respect to the parent sample of dwarf galaxies from I. Lazar et al. (2024a), we also plot the CAS parameters for the parent sample, obtained from the non-parametric analysis in HSC data, in the same plots (shown as grey data points). We expect some differences between the location of the parent sample in I. Lazar et al. (2024a) from the *HST* and *JWST* images presented here due to the differences in the PSF and wavelength changes, as already discussed earlier. This is indeed apparent from the plots in Fig. 8. In most cases, the CAS parameters derived from *HST*, NIRCam,

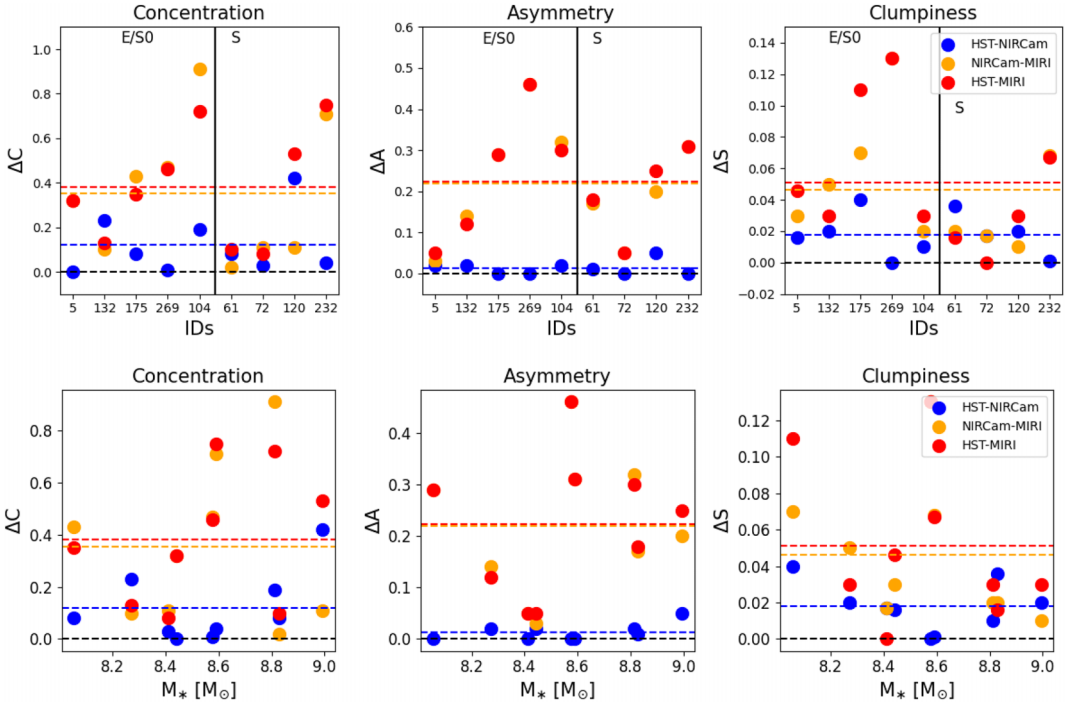

Figure 6. Change in the concentration (C, left panels), asymmetry (A, middle panels), and clumpiness (right panels) as a function of the morphological type in the top panels: early-type (E/S0) or late-type (S) and as a function of stellar mass in the bottom panels. Blue colour shows the difference in the CAS parameters between the *HST* and NIRCam images, orange shows the difference between NIRCam and MIRI images, and red shows the difference between *HST* and MIRI images. The black dotted line in all panels show the ΔCAS = 0 line and the blue, orange, and red dotted line show the average change for the *HST*–NIRCam, NIRCam–MIRI, and *HST*–MIRI images, respectively. Largest differences in the parameters are seen between *HST* or NIRCam versus MIRI images.

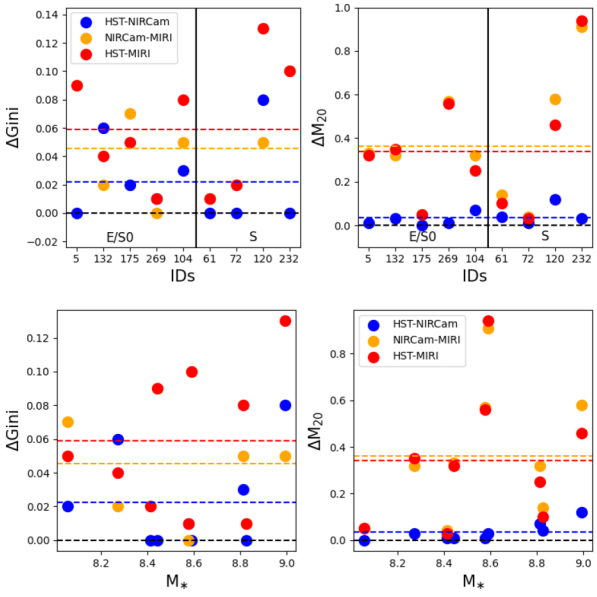

Figure 7. The figures show the change in Gini (ΔGini, left panels) and M_{20} (ΔM_{20}, right panels) with different data sets as a function of the morphological type (top panels) and stellar mass (bottom panels). Colour scheme of these plots is the same as Fig. 6.

and MIRI images reside in similar location as the parent sample of dwarf galaxies from I. Lazar et al. (2024a). A similar trend is observed in the M_{20} versus Gini coefficient parameter space in Fig. 9 i.e. the parameters derived from *HST*, NIRCam, and MIRI largely follow a similar locii as the parent I. Lazar et al. (2024a) sample. The most deviation in the CAS parameters or M_{20} and Gini parameters compared to I. Lazar et al. (2024a) data points is seen in the case of MIRI data, which, as we have already seen from Figs 5, 6, and 7, is most likely due to contribution from dust emission/clumps (see also Section 4.2.1), which become apparent at mid-infrared wavelengths, compared to optical or near-infrared wavelengths.

5 DISCUSSION

We presented multiwavelength imaging of nine dwarf galaxies from the COSMOS-Web survey, combining data from *HST*/ACS with *JWST*/NIRCam and MIRI. The high-sensitivity and depth of imaging surveys with new instruments aboard telescopes such as *JWST*, and even *Euclid*, is now allowing us to target larger samples of low-mass galaxies across a wide range of redshifts and in low-density environments (see F. R. Marleau et al. 2025; T. Shields et al. 2025). Two key findings emerge from the analysis presented in this paper: first, all dwarf galaxies in our sample (100 per cent) were detected with both NIRCam and MIRI. When comparing the observed fluxes to those predicted for low-mass galaxies in the TNG50 simulations, we find that the predicted mid-infrared fluxes from TNG50 are roughly consistent with the observed MIRI fluxes. Second, the morphological parameters of the dwarf galaxies exhibit a slight dependence on wavelength, with the most significant variations observed in the MIRI images compared to those from *HST* and NIRCam. The distinct appearance of the MIRI images possibly reflects the presence of dust lanes and clumps, which is also evident from the results of the

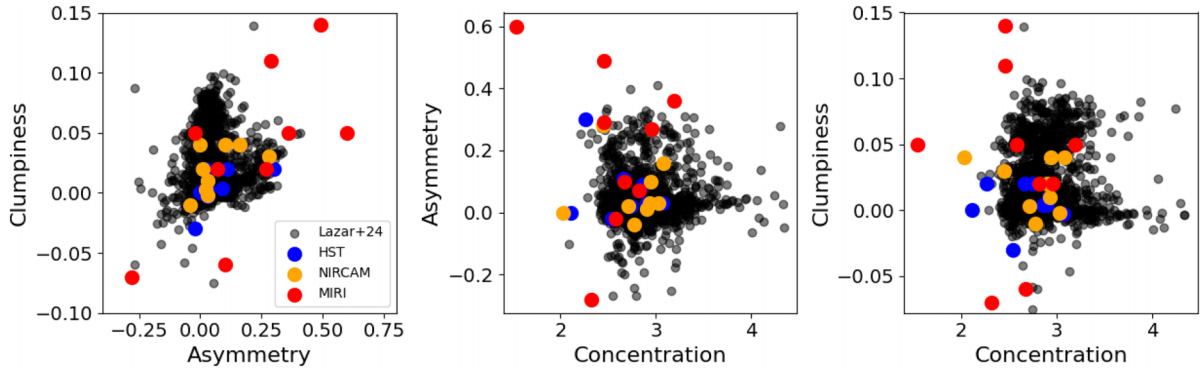

Figure 8. Location of the COSMOS-Web dwarf galaxies presented in this paper, with respect to the parent I. Lazar et al. (2024a) sample (background black circles) in different CAS parameter space. Blue, orange, and red circles show the morphological parameters determined from the *HST*/ACS *F*814*W*, *JWST*/NIRCam *F*277*W*, and *JWST*/MIRI *F*770*W* images, respectively. While most galaxies are within the locii of the I. Lazar et al. (2024a) sample, there is a noticeable change in the parameter location with wavelength.

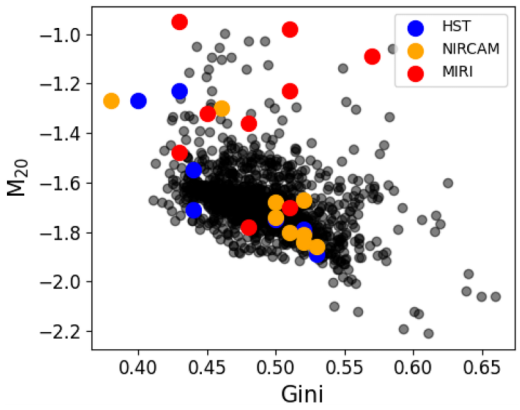

Figure 9. M20 versus Gini coefficient for the COSMOS-Web dwarf galaxies presented in this paper with respect to the parent I. Lazar et al. (2024a) sample. Colour scheme is the same as in Fig. 8. Similar to Fig. 8, the COSMOS-Web dwarfs approximately occupy the same locations as the parent sample.

SED modelling. In this section, we explore the implications of the analysis presented in this paper.

Broadly speaking, the mock fluxes derived from TNG50 simulations are dependent on: (1) the feedback prescriptions and the physics invoked in the TNG50 simulation itself, and (2) the RT implementation that assumes certain characteristics of the ISM, such as dust grain composition, dust-to-gas ratio, and metallicity dependence. We discuss here how the change in the nature of the feedback or in any of the assumptions in the post-processing might change the simulated fluxes. Within TNG50, galactic-scale winds from stellar feedback are sufficiently strong enough to disrupt the formation of disc or further accretion of gas on to host galaxies (see B. M. Celiz et al. 2025). However, these winds do not couple hydrodynamically with the surrounding ISM until they reach regions with densities below the star formation threshold (see G. Martin et al. 2025). Such a treatment of stellar feedback may not be sufficient to quench star formation on shorter timescales. On the other hand, AGN feedback in the radiatively inefficient regime is rather weak and does not have a strong impact on the ISM. Traditionally, AGN feedback is expected to play a crucial role in the evolution of massive galaxies. However, it has been shown recently that both AGN and stellar feedback may act simultaneously on dwarf galaxies (e.g. E. Arjona-Gálvez, A. Di Cintio & R. J. J. Grand 2021; S. Koudmani et al. 2022; R. S. Sharma et al. 2023). Therefore, the ISM content or composition can change significantly, depending whether a radiatively efficient AGN feedback model is included in simulations (e.g. M. Farcy et al. 2025).

In addition to feedback, RT applied to reproduce mock fluxes also includes several assumptions that may affect our results. This includes a change in dust-to-gas ratios, as higher dust content could result in a higher radiative efficiency and stronger outflows (e.g. A. C. Fabian, R. V. Vasudevan & P. Gandhi 2008). So, we first focus on one of the free parameters in the RT procedure, $f_{\rm dust}$, which represents the fraction of metallic gas confined in dust grains. As discussed in A. Trčka et al. (2022), this parameter varies across different samples in the literature and there are indications that $f_{\rm dust}$ depends on the metallicity, stellar mass, and/or redshift. The $f_{\rm dust} = 0.2$ is used for comparisons here, which is based on a median value from a sub-sample of galaxies from DustPedia galaxies (see P. De Vis et al. 2019), which have a stellar mass in the range $\log M_* = 8{-}11.5$ (the median stellar mass skewed towards higher stellar mass of $\sim 10^9$ $M_\odot$). The $f_{\rm dust}$ parameter shows a large scatter in the stellar mass range probed in this paper (fig. 11 in P. De Vis et al. 2019). The large scatter is also visible for low metallicity environments. We are unable to probe the dependence of $f_{\rm dust}$ on metallicity for this sample, as we do not have estimates for the latter. Dwarf galaxies are generally expected to have low dust content and low metallicity. Using lower values of dust-to-metal ratio for the diffuse dust, or higher covering fractions or lower H II region compactness in the MAPPINGS modelling of young stars may have resulted in lower mock MIRI fluxes (see L. Liang et al. 2021). However, the good agreement between modelled and observed fluxes suggest that these modelling choices are relatively sensible. The multiwavelength images and SED models presented in this paper clearly show that some of the dwarf galaxies presented here are abundant in dust. The SED models shown in Figs 4 and A3 also suggest excess contribution from diffuse dust and/or PAHs at mid-infrared wavelengths, compared to contribution from a stellar source modelled by a simple blackbody fit. In most galaxies, more than 50 per cent of the mid-infrared flux is estimated to be non-stellar origin, likely from warm or hot dust or PAHs, which is also evident from the best-fitting SED models in Figs 4 and A3.

The MIRI images of several dwarf galaxies show indications of dust lanes or clumps, when compared to the *HST* and NIRCam

images. In massive early-type galaxies, such dust lanes are usually indicative of previous merger activity with low mass companion galaxies (see S. Kaviraj et al. 2012; T. A. Davis et al. 2015), suggesting that these low mass dwarf galaxies might also have gone through a merger. Nearly 7 per cent of the massive ETGs show such dust features (e.g. S. Kaviraj 2010), compared to 22 per cent fraction we find in the dwarf galaxies (2/9). The incidence of dust lanes in our dwarf sample (in two sources: ID-5 and ID-175) is in contrast with 1 per cent reported in I. Lazar et al. (2024a). The multiwavelength data, especially the addition of MIRI imaging helps detect the spatial offsets, which may explain such differences between our work and I. Lazar et al. (2024a). The combination of *HST* + NIRCam + MIRI imaging of dwarf galaxies in low-density environments suggests that the contribution of dust grains at mid-infrared wavelengths can be significant in these low-mass galaxies. Rest-frame UV and/or optical spectroscopy would confirm if higher dust content would also correlate with higher gas-phase metallicity in these galaxies. The MIRI/*F*770*W* images also correspond to the 7.7 μm PAH emission, which may be stronger in some of the dwarfs presented here, as suggested by the best-fitting SED models of at least three dwarfs (ID-132, ID-175, and ID-232). If confirmed via mid-infrared spectroscopy, this would be in contrast with previous studies of BCDs or other nearby dwarf galaxies (e.g. S. C. Madden et al. 2006; L. K. Hunt et al. 2010), that show a lack of PAH emission.

Our results are similar to the findings of Y. Wu et al. (2006), who show the presence of PAH emission in BCDs using *Spitzer*/IRS spectroscopy (see also L. K. Hunt et al. 2010). Similarly, nearby dwarf galaxies (at distances <30 Mpc) in the *Spitzer* IRS Nearby Galaxies (SINGS) survey also reported the presence of dust emission and that the dust tends to be clumpy (e.g. D. A. Dale et al. 2007). However, other studies have also reported weakened PAHs and lower dust content in nearby dwarf galaxies (see review by F. Galliano, M. Galametz & A. P. Jones 2018). The typically low metallicities and weak PAH emission observed in dwarf galaxies may arise because PAHs are readily destroyed by intense UV radiation, while the small spatial scales of dwarf systems allow supernova-driven shocks to disperse PAHs globally, resulting in the characteristic PAH deficiency in low-metallicity galaxies (e.g. A. Rémy-Ruyer et al. 2015). We note that the studies described above largely focus on nearby dwarf galaxies or a special class of dwarf galaxies (BCDs), which may be biased towards higher SFRs and therefore, may not be representative of the broader dwarf population in low-density environments, such as the one discussed in this paper. Future mid-infrared spectroscopy with *JWST*/MIRI-MRS can provide strong constraints on the PAH composition in these dwarf galaxies.

Finally, the TNG50 galaxies are resolved into few gas elements at the lowest stellar masses; this may have implications for the robustness of the RT post processing. This is one limitation of the mock fluxes, in addition to other choices involved in the modelling of diffuse dust and young stars. Nevertheless, in spite of these caveats, from the comparisons shown in Fig. 3, we conclude that the 100 per cent detection rate of dwarf galaxies in the COSMOS-Web survey is not surprising and that the observed fluxes are approximately within the flux range expected from TNG50.

6 CONCLUSIONS AND FINAL REMARKS

We present high-resolution multiwavelength *HST* and *JWST* imaging observations of a sample of nine dwarf galaxies ($10^8 < M_*/M_\odot < 10^9$) selected from the COSMOS-Web survey. Here, we summarize the results of the analysis presented here:

(i) All dwarf galaxies in the sample are detected with both NIRCam and MIRI, corresponding to a 100 per cent detection rate. These galaxies exhibit a broad range of colours, SFRs, and stellar masses (M_*), with an approximately equal split between early-type and late-type morphologies. This suggests that the sample is broadly representative of dwarf galaxies found in low-density environments.

(ii) The observed NIRCam and MIRI fluxes align reasonably well with predictions from low-mass galaxies in the TNG50 simulation. This consistency implies that the feedback models and radiative transfer parameters used in post-processing are suitable for modelling such low-mass systems. Follow-up UV/optical spectroscopy will be essential for constraining the ionization parameter/structure, metallicity, metallicity gradient, SFR, and extinction within these galaxies.

(iii) The morphological parameters – CAS, M_{20}, and Gini – derived from *HST*, NIRCam, and MIRI data are generally consistent with those from the parent sample of I. Lazar et al. (2024a). Deviations are primarily seen in the MIRI-derived values, likely due to the influence of dust and/or the shallower depth of MIRI observations compared to NIRCam and *HST*. Owing to the diversity in the ISM properties of dwarf galaxies, we do not find a clear trend between these morphological parameters and the stellar mass or galaxy type. Surveys with future facilities such as Vera Rubin Observatory and *ROMAN* space telescope will be crucial to further explore the morphological diversity in a statistical sample of dwarf galaxies.

(iv) Mid-infrared MIRI observations strongly indicate the presence of dust in these dwarf galaxies, either in the form of dust clumps or dust lanes. Follow-up spectroscopy in near- and mid-infrared wavelengths using NIRSpec and MIRI–MRS will provide crucial constraints on the contribution to mid-infrared fluxes from PAHs, which will further provide detailed insights into the dust grain composition in these dwarf galaxies. MRS spectroscopy will also provide access to rotational transitions of hydrogen molecule and other ionization species, which will aid in constructing diagnostic diagrams to infer the molecular gas content and source of ionization in these dwarf galaxies.

ACKNOWLEDGEMENTS

We thank the anonymous referee for their constructive comments and suggestions. We thank M. Shuntov for providing us with the SED fits. SK, IL, and AEW acknowledge support from the STFC (grant numbers ST/Y001257/1 and ST/X001318/1). SK acknowledges a Senior Research Fellowship from Worcester College Oxford. IL and BB acknowledge PhD studentships funded by the Centre for Astrophysics Research at the University of Hertfordshire. RKC was grateful for support from the Leverhulme Trust via the Leverhulme Early Career Fellowship. SK has been supported by a Junior Research Fellowship from St Catharine's College, Cambridge and a Research Fellowship from the Royal Commission for the Exhibition of 1851. This research is based on observations made with the NASA/ESA *Hubble Space Telescope* obtained from the Space Telescope Science Institute, which is operated by the Association of Universities for Research in Astronomy, Inc., under NASA contract NAS 5-26555. These observations are associated with programmes 9822 and 10092. This work is based (in part) on observations made with the

NASA/ESA/CSA *James Webb Space Telescope*. The data were obtained from the Mikulski Archive for Space Telescopes at the Space Telescope Science Institute, which is operated by the Association of Universities for Research in Astronomy, Inc., under NASA contract NAS 5-03127 for *JWST*. These observations are associated with programme 1727.

DATA AVAILABILITY

The data used in this paper are available from the MAST portal (mast.stsci.edu) from the *HST* programme IDS 9822 and 10092 and *JWST* programme ID 1727.

REFERENCES

Abazajian K. et al., 2003, AJ, 126, 2081
Abraham R. G., van den Bergh S., Nair P., 2003, ApJ, 588, 218
Aihara H. et al., 2018, PASJ, 70, S8
Aihara H. et al., 2019, PASJ, 71, 114
Arjona-Gálvez E., Di Cintio A., Grand R. J. J., 2024, A&A, 690, A286
Ashby M. L. N. et al., 2018, ApJS, 237, 39
Atek H. et al., 2024, Nature, 626, 975
Baes M., Verstappen J., De Looze I., Fritz J., Saftly W., Vidal Pérez E., Stalevski M., Valcke S., 2011, ApJS, 196, 22
Bahcall N. A., Ostriker J. P., Perlmutter S., Steinhardt P. J., 1999, Science, 284, 1481
Bichang'a B., Kaviraj S., Lazar I., Jackson R. A., Das S., Smith D. J. B., Watkins A. E., Martin G., 2024, MNRAS, 532, 613
Bruzual G., Charlot S., 2003, MNRAS, 344, 1000
Bundy K. et al., 2015, ApJ, 798, 7
Bushouse H. et al., 2023, JWST Calibration Pipeline, Zenodo, doi:10.5281/zenodo.7795697
Bykov S. D., Gilfanov M. R., Sunyaev R. A., 2024, MNRAS, 527, 1962
Camps P., Baes M., 2015, Astron. Comput., 9, 20
Casey C. M. et al., 2023, ApJ, 954, 31
Celiz B. M., Navarro J. F., Abadi M. G., Springel V., 2025, A&A, 699, A12
Chabrier G., 2003, PASP, 115, 763
Cheng T.-Y. et al., 2021, MNRAS, 507, 4425
Conselice C. J., 2003, ApJS, 147, 1
Conselice C. J., 2014, ARA&A, 52, 291
Dale D. A. et al., 2006, ApJ, 646, 161
Dale D. A. et al., 2007, ApJ, 655, 863
Dashyan G., Silk J., Mamon G. A., Dubois Y., Hartwig T., 2018, MNRAS, 473, 5698
Davis T. A. et al., 2015, MNRAS, 449, 3503
Davis F. et al., 2022, MNRAS, 511, 4109
De Vis P. et al., 2019, A&A, 623, A5
Dekel A., Ostriker J. P. eds, 1999, Formation of Structure in the Universe,Cambridge University Press,Cambridge
Eigenthaler P. et al., 2018, ApJ, 855, 142
Faber S. M., Lin D. N. C., 1983, ApJ, 266, L17
Fabian A. C., Vasudevan R. V., Gandhi P., 2008, MNRAS, 385, L43
Farcy M. et al., 2025, MNRAS, 543, 967
Ferrarese L. et al., 2012, ApJS, 200, 4
Franco M. et al., 2025, preprint (arXiv:2506.03256)
Galliano F., Galametz M., Jones A. P., 2018, ARA&A, 56, 673
Glasse A. et al., 2015, PASP, 127, 686
Groves B., Dopita M. A., Sutherland R. S., Kewley L. J., Fischera J., Leitherer C., Brandl B., van Breugel W., 2008, ApJS, 176, 438
Harish S. et al., 2025, ApJ, 992, 45
Henkel C., Hunt L. K., Izotov Y. I., 2022, Galaxies, 10, 11
Hodges J. L., 1958, Arkiv for Matematik, 3, 469
Holwerda B. W. et al., 2014, ApJ, 781, 12
Hunt L. K., Thuan T. X., Izotov Y. I., Sauvage M., 2010, ApJ, 712, 164
Jackson R. A., Martin G., Kaviraj S., Laigle C., Devriendt J. E. G., Dubois Y., Pichon C., 2020, MNRAS, 494, 5568
Jackson R. A. et al., 2021, MNRAS, 502, 4262
Johnson B. D., Leja J., Conroy C., Speagle J. S., 2021, ApJS, 254, 22
Jones A. P., Köhler M., Ysard N., Bocchio M., Verstraete L., 2017, A&A, 602, A46
Kaviraj S., 2010, MNRAS, 406, 382
Kaviraj S. et al., 2012, MNRAS, 423, 49
Kaviraj S., Martin G., Silk J., 2019, MNRAS, 489, L12
Kaviraj S., Lazar I., Watkins A. E., Laigle C., Martin G., Jackson R. A., 2025, MNRAS, 538, 153
Koekemoer A. M. et al., 2007, ApJS, 172, 196
Kormendy J., Ho L. C., 2013, ARA&A, 51, 511
Koudmani S., Sijacki D., Smith M. C., 2022, MNRAS, 516, 2112
Kumari N., James B. L., Irwin M. J., Aloisi A., 2019, MNRAS, 485, 1103
Kunth D., Maurogordato S., Vigroux L., 1988, A&A, 204, 10
Lazar I., Kaviraj S., Watkins A. E., Martin G., Bichang'a B., Jackson R. A., 2024a, MNRAS, 529, 499
Lazar I., Kaviraj S., Watkins A. E., Martin G., Bichang'a B., Jackson R. A., 2024b, MNRAS, 533, 3771
Lequeux J., Peimbert M., Rayo J. F., Serrano A., Torres-Peimbert S., 1979, A&A, 80, 155
Liang L., Feldmann R., Hayward C. C., Narayanan D., Çatmabacak O., Kereš D., Faucher-Giguère C.-A., Hopkins P. F., 2021, MNRAS, 502, 3210
Loose H.-H., Thuan T. X., 1986 ApJ 309 59
Lotz J. M., Primack J., Madau P., 2004, AJ, 128, 163
Madden S. C., Galliano F., Jones A. P., Sauvage M., 2006, A&A, 446, 877
Marinacci F. et al., 2018, MNRAS, 480, 5113
Marleau F. R. et al., 2025, preprint (arXiv:2503.15335)
Martin G., Kaviraj S., Devriendt J. E. G., Dubois Y., Pichon C., 2018, MNRAS, 480, 2266
Martin G. et al., 2021, MNRAS, 500, 4937
Martin G. et al., 2025, MNRAS 541 1831–1850
McConnachie A. W., 2012, AJ, 144, 4
McCracken H. J. et al., 2012, A&A, 544, A156
Mezcua M., Suh H., Civano F., 2019, MNRAS, 488, 685
Mezcua M., Pacucci F., Suh H., Siudek M., Natarajan P., 2024, ApJ, 966, L30
Naiman J. P. et al., 2018, MNRAS, 477, 1206
Nelson D. et al., 2019, MNRAS, 490, 3234
Papaderos P., Loose H. H., Thuan T. X., Fricke K. J., 1996, A&AS, 120, 207
Partmann C., Naab T., Rantala A., Genina A., Mannerkoski M., Johansson P. H., 2024, MNRAS, 532, 4681
Peng Y.-j., Maiolino R., 2014, MNRAS, 438, 262
Petersson J. et al., 2025, A&A, 704, A177
Pillepich A. et al., 2019, MNRAS, 490, 3196
Reaves G., 1983, ApJS, 53, 375
Rémy-Ruyer A. et al., 2015, A&A, 582, A121
Rest A., Pierel J., Correnti M., Hilbert B., Canipe A., Sunnquist B., Fox O., 2023, The JWST HST Alignment Tool (JHAT), Zenodo, doi:10.5281/zenodo.7892935
Rieke M. J. et al., 2023, PASP, 135, 028001
Rodriguez-Gomez V. et al., 2019, MNRAS, 483, 4140
Sánchez-Janssen R., Aguerri J. A. L., Muñoz-Tuñón C., 2008, ApJ, 679, L77
Sandage A., Binggeli B., 1984, AJ, 89, 919
Sawicki M. et al., 2019, MNRAS, 489, 5202
Schreiber C. et al., 2015, A&A, 575, A74
Scoville N. et al., 2007, ApJS, 172, 1
Sharma R. S., Brooks A. M., Tremmel M., Bellovary J., Quinn T. R., 2023, ApJ, 957, 16
Shields T. et al., 2026, MNRAS preprint (arXiv:2511.17738)
Shuntov M. et al., 2025, A&A, 704, A339
Springel V., 2010, MNRAS, 401, 791
Springel V. et al., 2018, MNRAS, 475, 676
Taniguchi Y. et al., 2015, PASJ, 67, 104
Tempel E., Tago E., Liivamägi L. J., 2012, A&A, 540, A106
Tolstoy E., Hill V., Tosi M., 2009, ARA&A, 47, 371

Torrey P., Vogelsberger M., Sijacki D., Springel V., Hernquist L., 2012, MNRAS, 427, 2224
Torrey P. et al., 2019, MNRAS, 484, 5587
Tremonti C. A. et al., 2004, ApJ, 613, 898
Trujillo I. et al., 2021, A&A, 654, A40
Trčka A. et al., 2022, MNRAS, 516, 3728
van den Bergh S., 1998, Galaxy Morphology and Classification,Cambridge University Press,Cambridge
Venhola A. et al., 2019, A&A, 625, A143
Vogelsberger M., Marinacci F., Torrey P., Puchwein E., 2020, Nature Reviews Physics, 2, 42
Watkins A. E., Martin G., Kaviraj S., Collins C., Dubois Y., Kraljic K., Pichon C., Yi S. K., 2025, MNRAS, 537, 3499
Weaver J. R. et al., 2022, ApJS, 258, 11
Weinberger R., Springel V., Pakmor R., 2020, ApJS, 248, 32
Weisz D. R., Dolphin A. E., Skillman E. D., Holtzman J., Gilbert K. M., Dalcanton J. J., Williams B. F., 2014, ApJ, 789, 147
Wright A. H. et al., 2017, MNRAS, 470, 283
Wright G. S. et al., 2023, PASP, 135, 048003
Wu Y., Charmandaris V., Hao L., Brandl B. R., Bernard-Salas J., Spoon H. W. W., Houck J. R., 2006, ApJ, 639, 157
Zamojski M. A. et al., 2007, ApJS, 172, 468

APPENDIX A: APPENDIX

Table A1. Parametric and non-parametric morphological analysis of the dwarf galaxies presented in this paper. The notations are the same as in Table 2.

ID	*HST*/ACS						NIRCam						MIRI					
	n	C	A	S	M_{20}	Gini	n	C	A	S	M_{20}	Gini	n	C	A	S	M_{20}	Gini
5	1.0	2.90	0.03	0.004	−1.80	0.52	1.0	2.90	0.01	0.02	−1.81	0.52	0.9	2.58	−0.02	0.05	−1.48	0.43
61	1.0	2.54	−0.02	−0.03	−1.71	0.44	1.0	2.77	−0.04	−0.01	−1.68	0.50	1.0	2.67	0.10	−0.06	−1.36	0.48
72	0.6	1.78	0.0	0.0	−1.27	0.23	0.5	2.03	0.00	0.04	−1.27	0.38	0.6	2.46	0.29	0.11	−1.32	0.45
104	1.1	2.92	0.03	0.01	−1.79	0.52	1.0	2.93	0.03	0.01	−1.80	0.51	0.5	2.46	0.49	0.14	−1.23	0.51
120	0.7	2.26	0.30	0.02	−1.23	0.43	0.7	2.45	0.28	0.03	−1.30	0.46	0.8	1.54	0.60	0.05	−0.98	0.51
132	1.1	2.86	0.09	0.004	−1.80	0.52	1.1	2.94	0.10	0.04	−1.84	0.52	1.1	2.96	0.27	0.02	−1.70	0.51
175	0.9	2.74	0.02	0.02	−1.75	0.50	0.8	2.71	0.02	0.003	−1.74	0.50	0.8	2.82	0.07	0.02	−1.78	0.48
232	0.8	2.66	0.11	0.02	−1.55	0.44	0.9	3.08	0.16	0.04	−1.67	0.52	1.0	3.19	0.36	0.05	−1.09	0.57
269	1.2	3.07	0.03	−0.003	−1.89	0.53	1.1	3.03	0.03	−0.002	−1.86	0.53	1.2	2.32	−0.28	−0.07	−0.95	0.43
Avg	0.9	2.67	0.10	0.006	−1.65	0.48	0.9	2.79	0.14	0.019	−1.67	0.51	1.0	2.61	0.20	0.023	−1.37	0.50

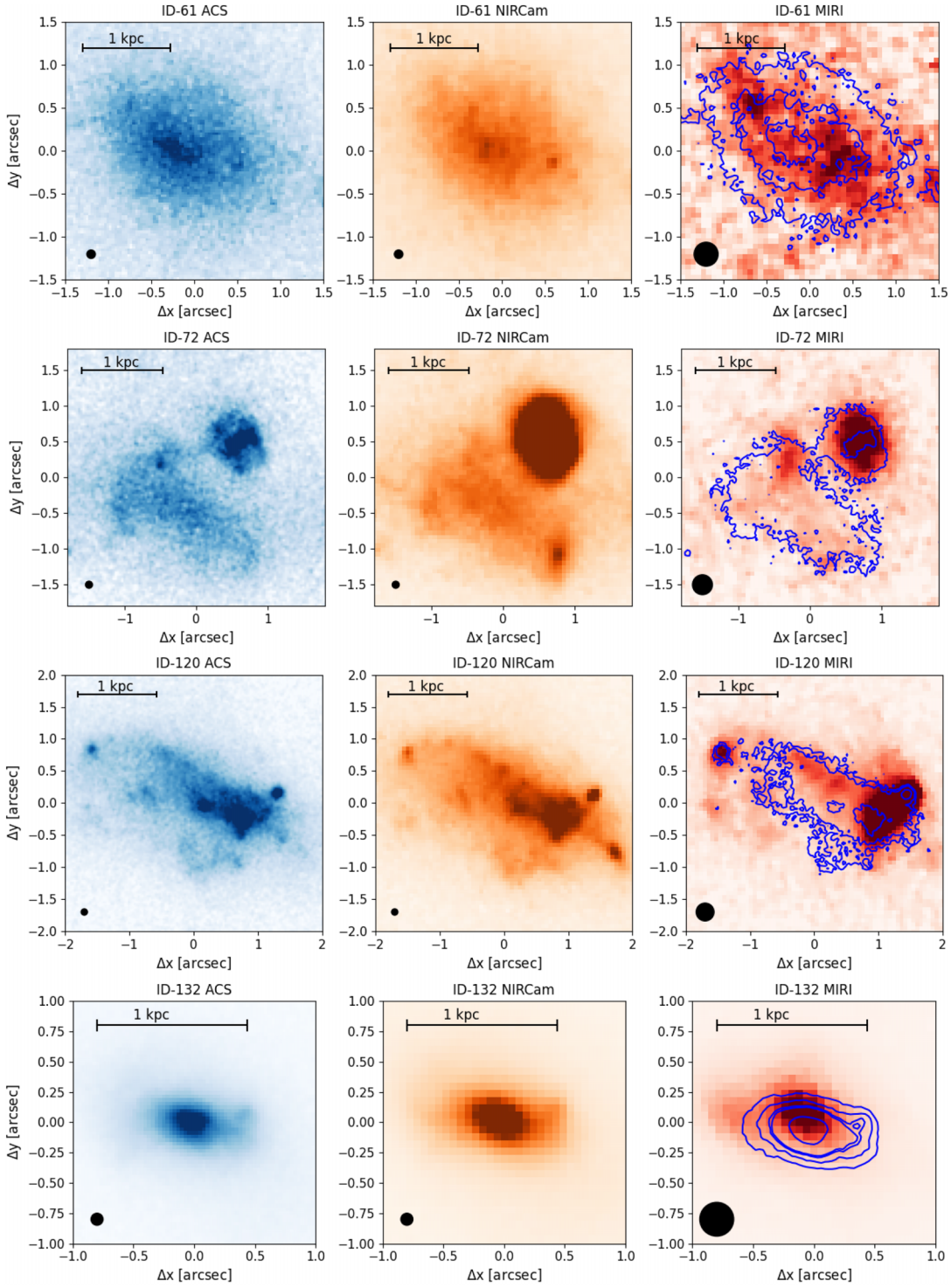

Figure A1. From top to bottom: ID 61, 72, 120, and 132.

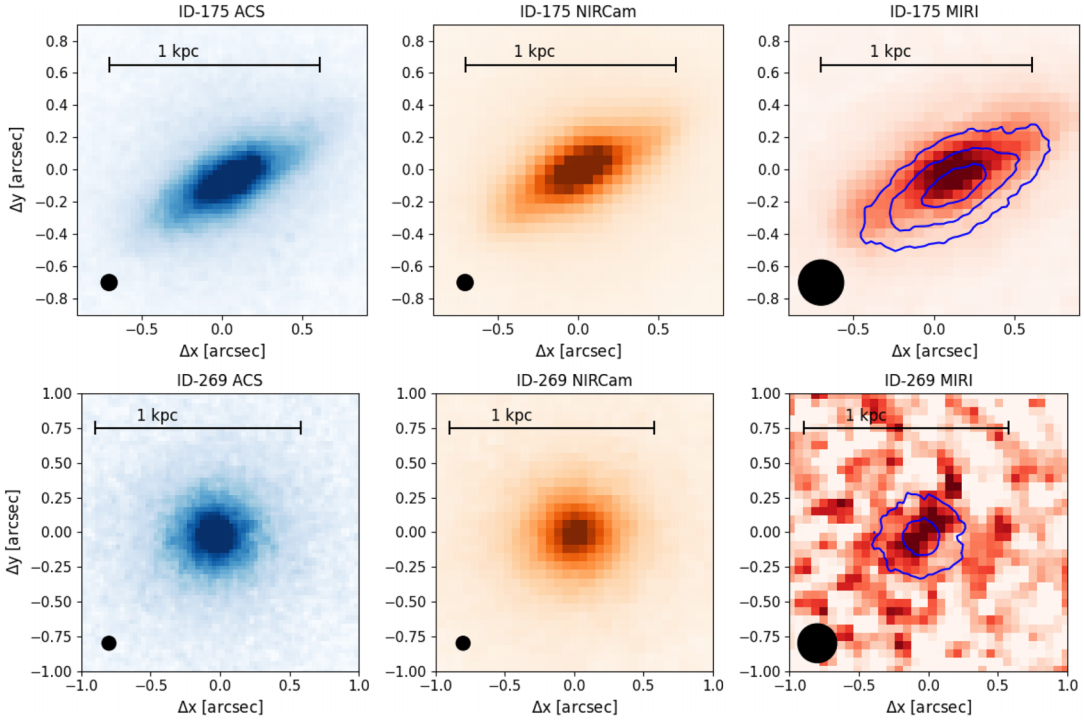

Figure A2. From top to bottom: ID 175 and 269.

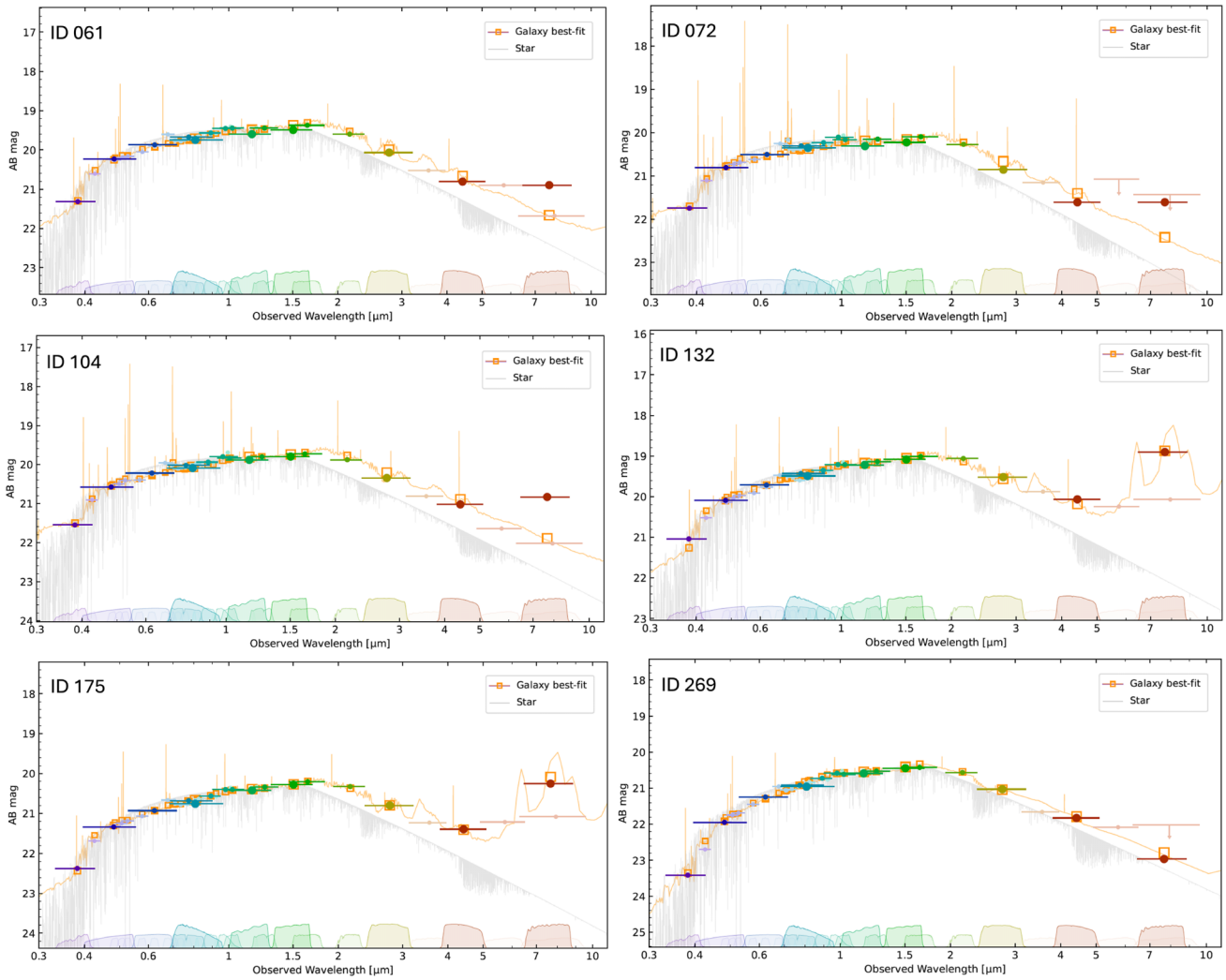

Figure A3. SED fits of the rest of the targets in this paper. The colour scheme is the same as Fig. 4.

[1]*Centre for Astrophysics Research, Department of Physics, Astronomy and Mathematics, University of Hertfordshire, Hatfield AL10 9AB, UK*
[2]*Laboratory for Multiwavelength Astrophysics, School of Physics and Astronomy, Rochester Institute of Technology, 84 Lomb Memorial Drive, Rochester, NY 14623, USA*
[3]*Jodrell Bank Centre for Astrophysics, University of Manchester, Oxford Road, Manchester M13 9PL, UK*
[4]*School of Physics and Astronomy, University of Nottingham, University Park, Nottingham NG7 2RD, UK*
[5]*St Catharine's College, University of Cambridge, Trumpington Street, Cambridge CB2 1RL, UK*
[6]*International Centre for Radio Astronomy Research, University of Western Australia, 7 Fairway Crawley, WA 6009,Australia*
[7]*Research School of Astronomy and Astrophysics, Australian National University, Canberra, ACT 2611, Australia*
[8]*ARC Centre of Excellence for All Sky Astrophysics in 3 Dimensions (ASTRO 3D), Canberra, ACT2611,Australia*
[9]*Department of Astronomy, The University of Texas at Austin, 2515 Speedway Blvd Stop C1400, Austin, TX 78712, USA*
[10]*Department of Physics, University of California, Santa Barbara, CA 93106, USA*
[11]*Cosmic Dawn Center (DAWN), Rådmandsgade 64, 2200 København N.,Denmark*
[12]*Université Paris-Saclay, Université Paris Cité, CEA, CNRS, AIM, F-91191 Gif-sur-Yvette, France*
[13]*Department of Computer Science, Aalto University, PO Box 15400, FI-00076 Espoo, Finland*
[14]*Department of Physics, University of Helsinki, PO Box 64, FI-00014 Helsinki, Finland*
[15]*Institute of Physics, Lab for Galaxy Evolution, EPFL, Observatoire de Sauverny, Chemin Pegasi 51, CH-1290 Versoix, Switzerland*
[16]*Department of Physics and Astronomy, University of Kentucky, 505 Rose Street, Lexington, KY 40506, USA*
[17]*Space Telescope Science Institute, 3700 San Martin Drive, Baltimore, MD 21218, USA*
[18]*Purple Mountain Observatory, Chinese Academy of Sciences, 10 Yuanhua Road, Nanjing 210023, China*
[19]*Institut d'Astrophsyique de Paris, UMR 7095, CNRS, UPMC Univ., Paris VI 98 bis boulevard Arago, 75014 Paris, France*
[20]*Jet Propulsion Laboratory, California Institute of Technology, 4800 Oak Grove Drive, Pasadena, CA 91001, USA*
[21]*Department of Astronomy and Astrophysics, University of California, Santa Cruz, 1156 High Street, Santa Cruz, CA 95064, USA*

This paper has been typeset from a TEX/LATEX file prepared by the author.